Supplementary Information for Collective optical behavior from coupled quantum dots visualized by wavelength-resolved and polarization-resolved super-resolution microscopy

Duncan P. Ryan[1,*], *Megan K. Dunlap*[2], *Jennifer A. Hollingsworth*[1], *Somak Majumder*[1], *Martin P. Gelfand*[3], *James H. Werner*[1], *Alan van Orden*[2], *and Peter M. Goodwin*[1]

[1]Center for Integrated Nanotechnologies, Los Alamos National Laboratory, Los Alamos, New Mexico, 87545, USA
[2]Department of Chemistry, Colorado State University, Fort Collins, Colorado, 80523, USA
[3]Department of Physics, Colorado State University, Fort Collins, Colorado, 80523, USA
[*]E-mail: ryand@lanl.gov

I QD characterization

CdSe/CdS core/shell QDs were synthesized according to procedures described by Chen, *et al.*[1] Figure S1a illustrates a representative TEM image of the final particles. This protocol utilizes slow growth to produce high-quality QDs. Particles were faceted with narrow shape and size distributions. The ensemble emission profile, Fig. S1b, is a single emission wavelength centered at 636 nm. The single-particle spectral bandwidth reported in[1] is $\sigma = 10.2$ nm while the ensemble emission profile has a spectral width of $\sigma = 14.5$ nm, indicating a narrow distribution of emission centers. When assembled into nanoassemblies, this distribution of wavelengths results in some particles taking on the role of donors and others acceptors for energy transfer. Figure S1c shows the distribution of CdSe sizes after core synthesis and the distribution of the final QD sizes after capping with CdS shells. In the size regime below 10 nm, QD-QD separation distances after clustering can be small enough to facilitate energy transfer with modest to low efficiency. Therefore, emission from donor QDs are not completely quenched and can be substantial enough to provide robust fluorescence localization.

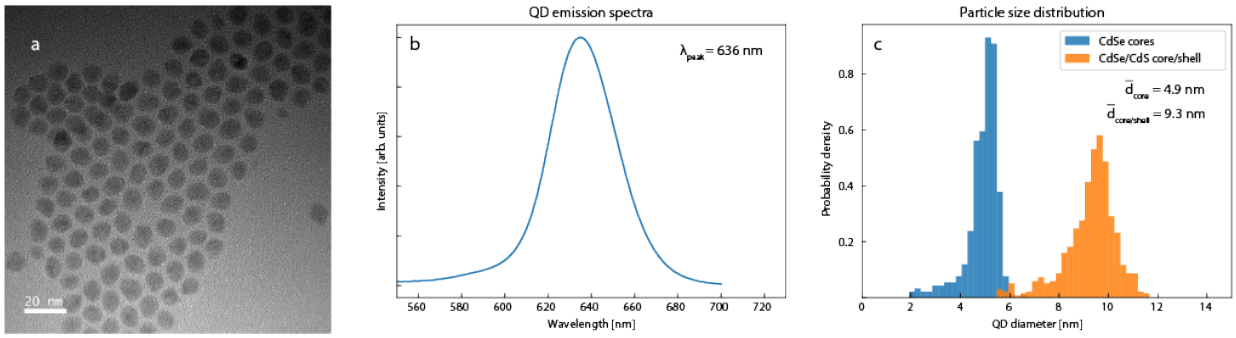

Figure S1: **QD characterization.** **a,** TEM image of QD sample. The aggregation shown is due to the drying, wicking individual QDs together, and is a different clustering/concentrating process than the one used to form nanoassemblies for optical imaging experiments. Additionally, inter-particle gaps are not present in QD nanoassemblies. **b,** Emission profile of QD sample. Ensemble peak emission was 636 nm. **c,** Histogram of QD diameters measured from TEM images. 578 QDs were used to generate the core/shell probability distribution.

II Rotation consistency

To demonstrate the instrumentation and analysis methods of dual-color polarization microscopy are sensitive to expected orientation changes, a sample of QDs was imaged in two known orientations. QDs were imaged in an initial orientation, the sample was unmounted from the microscope, rotated 90° counter-clockwise, remounted, and the same constellation of QDs imaged a second time with the different orientation. Figure S2 shows orientation analysis results for a representative QD. The orientation features, initially aligned north-south (along y-axis in sample plane), were rotated to east-west (along x-axis in sample plane) in the physically rotated image series. The minor discrepancy of the polar angle θ changing is within the uncertainty and scatter of the two measurements. Additionally, the physical rotation moved spots into different regions of the FOV. Different channel correction factors were necessarily applied based on the translated spot locations. The consistency of expected orientation signatures further demonstrates the analysis methods required to extract accurate orientation information about an emitter.

Although the QDs presented in this work generally exhibited similar azimuthal angles ϕ, this appears to be coincidental. As shown in Figs. S2 and S15, other orientations were observed, but were uncommon in the datasets presented in this study.

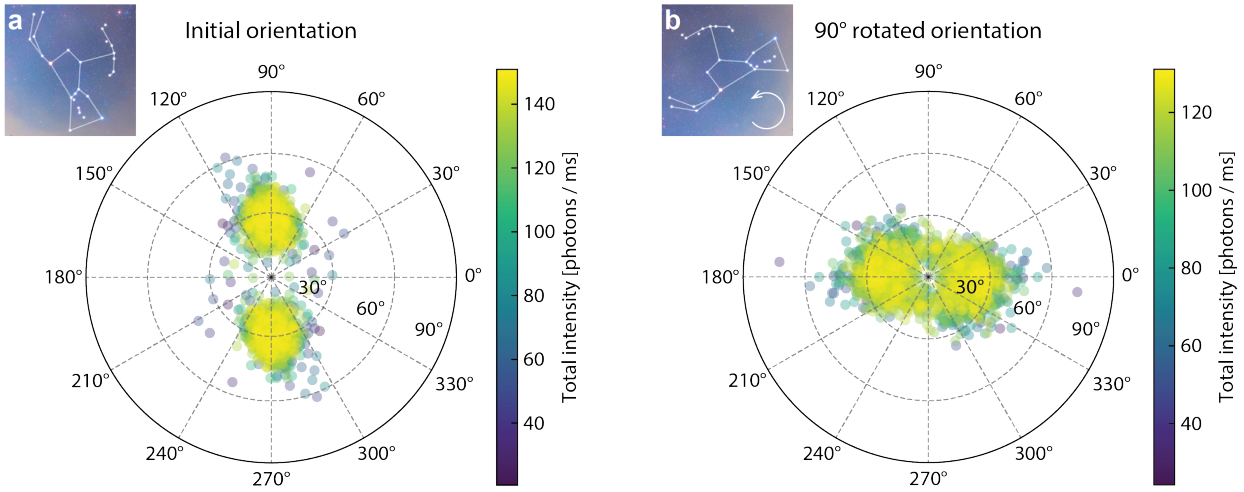

Figure S2: **Sample rotation. a,** Orientation projection of a single QD as initially mounted on microscope. **b,** Orientation projection of the same QD after the coverslip was rotated 90° counter-clockwise and remounted. The orientation information extracted from polarization measurements correctly registered the physical rotation of the sample.

III Orientation analysis

While the azimuthal angle ϕ of an emitter can be obtained directly from the Stokes parameters S_0, S_1, and S_2 up to a degeneracy of 180°, the polar angle θ requires a more comprehensive description of the imaging system and the emitter itself. Lethiec *et al.*[2] formulated a model describing the polarized emission generated by 1D and 2D dipole emitters in various imaging configurations. In that work, the signal modulations generated by a rotating analyzer setup is related to θ through

$$P_{1D}(\theta) = \frac{C \sin^2\theta}{(2A - 2B + C)\sin^2\theta + 2B}$$

$$P_{2D}(\theta) = \frac{C \sin^2\theta}{-(2A - 2B + C)\sin^2\theta + 4A + 2C}$$

where the variables A, B, and C are given in [2] and are dependent on parameters of the imaging system. Figure S3a shows the dependence of the modulation depth on the tilt angle θ of the emitter. The use of a high-NA objective and the 2D nature of the emission restrict the range of modulation depths that can be observed. The camera-based configuration presented in this work measures signals from four fixed analyzer angles. While the analysis framework by Lethiec *et al.* is based on a continuously rotated analyzer, the theory may be applied to other setups. The Stokes polarization factor p measured by a camera-based experiment is equivalent to the modulation depth of a rotating analyzer.

The nature of the dipole emission from semiconductor QDs has seen modest attention in

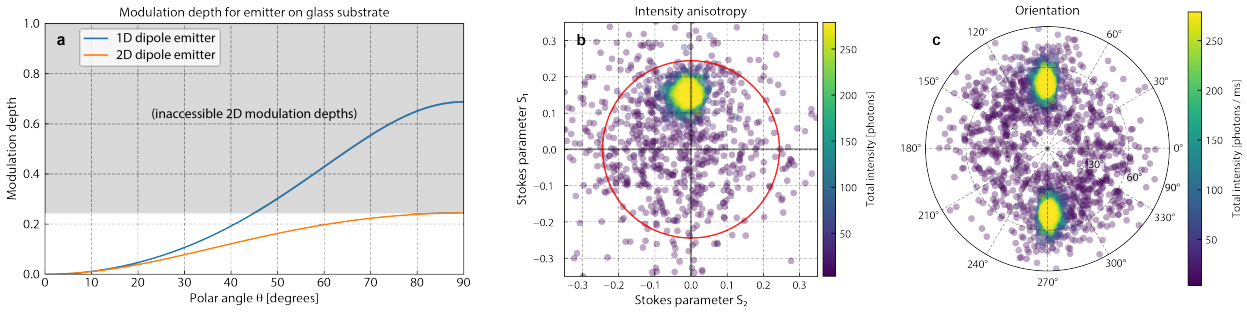

Figure S3: **Polar angle calculation. a,** Calibration curves from Lethiec model for a 1D (blue) and 2D (orange) dipole emitter. The models were calculated for an emitter with emission at 630 nm located on the glass/air interface of a coverslip (index of refraction $n = 1.518$) and with the emission collected by a 1.50 NA objective. Given the high NA of the objective, modulation depths among the polarization channels are limited. For 2D dipole emitters, such as QDs, modulation depths greater than ~ 0.25 are not predicted by the model. **b,** After applying corrections for the optical path efficiencies, anisotropy values among orthogonal polarization intensity pairs were calculated to determine orientation. Correlation plots of the two anisotropy values (rotated and non-rotated polarization optical paths) determine the final orientation: the angle relative to the x-axis indicates $\phi/2$, and the radius corresponds to the modulation depth. The model in **a** is used to calculate θ. The red circle indicates the maximum radius/modulation depth for the model of a 2D emitter. Measurements beyond this radius cannot be converted into angles. **c,** The orientation depiction of the data in **b**.

literature[3–7]. QDs are generally categorized as 2D dipole emitters. However, evidence for elliptical 2D emission[4] and 2D+1D transition moments[6] has been shown. These studies combined polarization anisotropy measurements and defocused imaging, demonstrating the anisotropy method of measuring orientation can be skewed for QD systems with complex dipole moments. While defocused imaging can elucidate the nature of the dipole emission, super-resolution localization precision suffers as a result. The CdSe/ZnS semiconductor system (different capping shell than this work) has been the most extensively studied for these complex signatures, and lattice strain has been identified as impacting fluorescence behaviors in this system[8, 9]. Poor-quality QDs can exhibit polycrystallinity and have irregular shapes, further complicating emission polarization. However, the CdSe/CdS system exhibits less lattice strain due to mismatch, and the QDs in this work were synthesized with a slow growth protocol that produced high-crystalline purity and regular shapes. Lethiec, *et al.*[2] demonstrated CdSe/ZnS QDs may be 2D+1D, but the distribution of anisotropy measurements from CdSe/CdS QDs fit the model for 2D emission. Thus, the application of the 2D emission model is justified for the QDs in this study.

Figure S3 illustrates the steps to calculate orientation (θ and ϕ) from the Stokes anisotropy parameters (S_1 and S_2). Analysis for a single QD is shown. The range of valid modulation depths for a 2D emitter is indicated in Fig. S3a, which is represented by a red circle in the

correlation plot of the Stokes anisotropy parameters, Fig. S3b. The angle of a marker relative to the positive x-axis indicates $\phi/2$ and the radius is a measure of the modulation depth (*i.e.* the Stokes polarization parameter p). All individual QDs and QD nanoassemblies studied in this work exhibited polarization parameters smaller than the maximum predicted for a 2D emitter. Figure S3c shows the mapping of the radial and angular components of the anisotropy plot onto the 2D dipole emission model, producing the orientation plot.

IV Spectral calibration

To calculate the spectral signature from the distribution of intensities into the red and blue channels of a given polarization component, we followed the procedure outlined in[10] with modifications for the two passes of the dichroics. After encountering the second dichroic beamsplitter, a fraction of the photons are lost because they do not continue along an imaging path. Thus, the spectral response functions $f_i^2(\lambda)$ serve to determine the photon flux into the detection arm of the microscope, increasing intensity estimates to account for losses from the dichroic beamsplitters. The polarization components separated by the polarization optics are aligned along either the S- or P-polarization directions of the dichroic optics (see Fig. 1). Thus, the spectral response functions must correspond to the appropriate S- or P-polarization for analysis. The manufacturer spectral response curves for the 624 dichroic beamsplitters (Semrock) were used for spectral calculations. Figure S4a shows the transmission of the dichroics for S- and P-polarization after convolution with the bandwidth of a single QD. The single-pass (dashed) and double-pass (solid) transmission curves are displayed, illustrating the losses from uncollected light, but only the double-pass curves are used for analysis. Because of losses, reflection curves are not complimentary functions to the transmission curves. That is,

$$\mathrm{R}_i \equiv \left(1 - f_i(\lambda)\right)^2 \leq 1 - f_i^2(\lambda)$$

Following the procedure in[10], spectral response functions are used to generate calibration curves that map measured intensities of the red and blue channels onto wavelength. Figure S4b shows the calibration curves for single- and double-pass of the dichroics. If the double-pass is not considered, the calibration curve can result in spectral errors in excess of 5 nm. Furthermore, the spectral anisotropy value η has a more limited range if only single-passes are considered than when two passes are considered. Among the QDs studied in this work, η values that could only be valid with the double-pass treatment of the spectral response function were frequently encountered.

The raw wavelength calculation (see Spectral analysis in the Methods section) and the spectral-intensity distributions shown in this work use an approximation of the calibration curves presented in Fig. S4b to depict the uncertainty associated with the spectral calculations. Reference[10] discusses the process and accuracy of the approximation. S- and

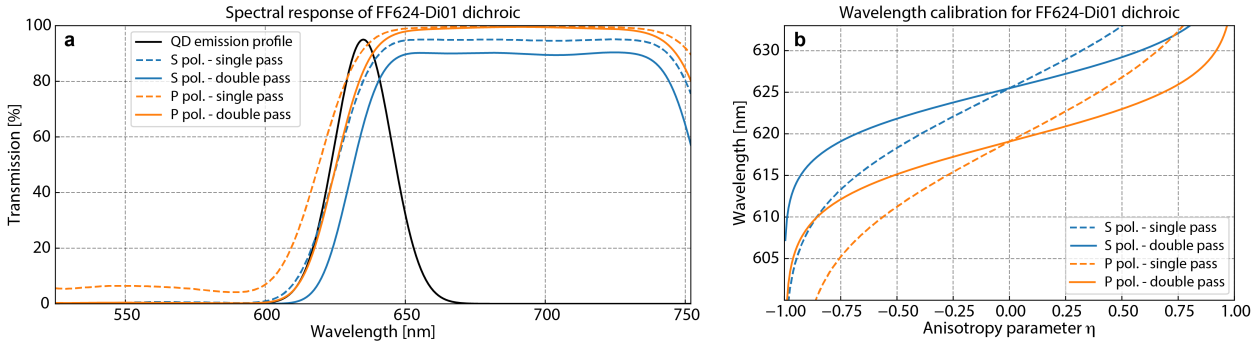

Figure S4: **Dichroic calibration. a,** Theoretical S-polarization (blue) and P-polarization (orange) response curves of the 624 dichroic beamsplitters. The responses of single transmission passes are shown as dashed lines, and the system responses after two passes are shown as solid lines. The 10.2 nm spectral bandwidth of the QDs is shown in black for reference. **b,** Wavelength calibration curves for the S polarization (blue) and the P polarization (orange) signals using the spectral response curves of **a**. If only a single transmission/reflection pass is considered, the calibration curves (dashed lines) are significantly different and have smaller ranges of valid anisotropy values η. The double-pass curves (solid lines) were used to calibrate spectral features in this work and encompass η ranges that were found in the experimental data.

	$a \approx \lambda_{\mathrm{Di}}$ [nm]	$b \approx \sqrt{2}\sigma$ [nm]	$c \approx 1$	$d \approx 0$
S polarization	625.51	7.95	1.005	-9.77×10^{-4}
P polarization	619.01	8.46	1.012	1.12×10^{-3}

Table S1: Parameters for the analytical expression of wavelength. The parameters were determined from fitting the approximation expression to the wavelength calibration curves generated from the spectral response functions.

P-polarization channels require different parameter sets for the approximation. Table S1 summarizes these parameter sets, determined from the spectral response functions of the 624 nm dichroic beamsplitters.

The application of the spectral calibration to a single QD is shown in Fig. S5. Scatter plots of the intensity and spectral anisotropy η for each polarization component (top row, a–d) illustrate the first step of the spectral calculation. Each marker indicates the results from a single frame. Spectral-intensity distributions (bottom row, e–h) apply the spectral calibration curves (Fig. S4) to the anisotropy data, compiling the results from individual frames into a probability map that incorporates the uncertainty of the intensity and spectral calculations, as well as the frequency a given emission state was visited.

A grouping of the spectral signatures of the two S-polarization channels and the two P-

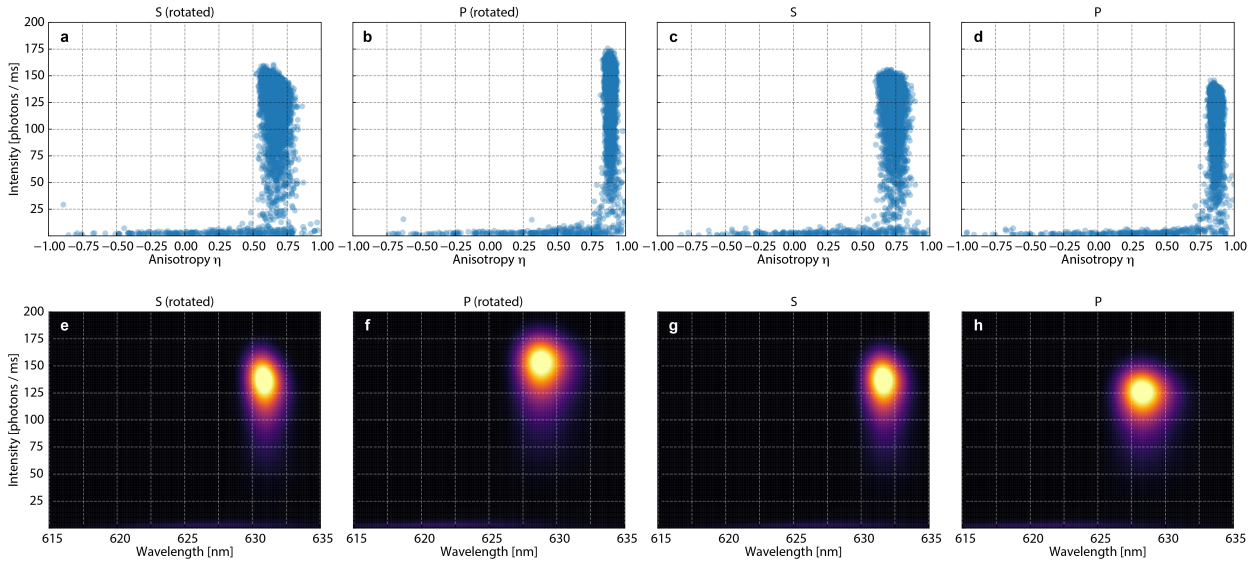

Figure S5: **Spectral calibration. a–d,** The raw anisotropy values η from comparing blue/red channel intensities of each polarization optical path for the single QD example in the manuscript. Because of the different S/P polarization response curves of the dichroic beamsplitters, the two S optical paths (rotated and non-rotated) are similar to each other but different from the P optical paths. **e–h,** Spectral-intensity distributions of the same QD for each polarization optical path. After applying the relevant calibration curve (see Fig. S4b), the spectral features look more consistent across all polarization optical paths. The widths of the distributions are also similarly matched across the different paths.

polarization channels was observed. P-polarization channels generate wavelength signatures $\sim$3.5 nm shorter than the S-polarization channels in Fig. S5e–h. This discrepancy is due to the change of dichroic response as a function of the angle of incidence (AOI). To separate the polarization images on the cameras, small propagation angles are introduced into each path with the turning mirrors located before the polarizing beamsplitter. Therefore, the AOIs on the dichroic beamsplitters are $45° \pm \gamma$, where γ is small. The transition wavelengths of the dichroics are linear with AOI near 45°. This feature manifests as a small wavelength offset in each polarization channel. Without incorporating the AOIs explicitly into the spectral response functions $f_i^2(\lambda)$, the true wavelength of an emitter is the average of the S- and P-polarization results because the AOIs and angular responses are symmetric around 45°. An additional contributing factor to the discrepancies is that the spectral calculations do not apply corrections related to the optical path efficiencies. However, the red channel of a given polarization component is imaged onto one camera and the blue channel is imaged onto the other camera. Differences of dirt on the sensor, sensor quantum efficiency, and camera gain calibration can impact spectral results. However, these effects are less significant than AOI considerations.

A summary of the median wavelength and peak emission intensity for 20 single QDs

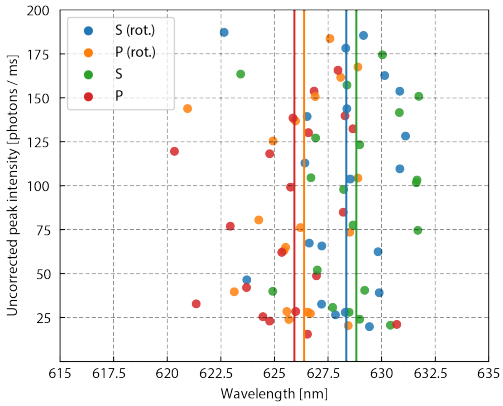

Figure S6: **Spectral characterization of single QDs.** The distribution of single QD spectral and intensity features to demonstrate single-particle characterization of the QD sample batch. Each marker represents the median wavelength and peak emission intensity over the duration of 4,000 frames for an individual QD.

is shown in Fig. S6, illustrating the distribution of emission properties for a collection of particles. Such spectral variation shows how donor/acceptor roles emerge from a batch of the same species of QDs, despite the monodisperse QD sample. The polarization component sample averages are indicated by solid lines and demonstrate the same grouping between S- and P-polarizations as described previously. We note that the average wavelength from single particle measurements is ∼10 nm shorter than the in-solution ensemble characterizations shown in Fig. S1. Studies have reported no significant spectral shifts between toluene ensemble measurements and QDs embedded in PMMA[11]; however, QDs in air were not examined and ligands specific to the Chen *et al.*[1] synthesis method were not investigated.

V Optical path efficiency corrections

Correction factor maps calculated from QD films (see Methods section) are shown in Fig. S7 for two imaging configurations: polarization-only measurements and dual-color polarization measurements. For the former, the dichoric beamsplitters necessary to determine emitter wavelength were not installed, and, for the latter, the dichroics were installed, requiring the additional spectral considerations described above. In all configurations and polarization components there were regions within the FOVs that required non-trivial corrections to calculate orientation from intensity information. The non-uniform correction factors across the FOVs can be due to a variety of factors, including: clipping/occultation along the optical paths from optical mounts, imperfect intensity splitting from the 50/50 and polarizing beamsplitters, non-uniform transmission through optical elements such as lenses due to dirt, and the spectral and polarization responses of individual optical elements. Blue channels require the most significant corrections for both S- and P-polarization components. To

the best of our knowledge, generating calibration maps that consider spatial variation, as opposed to single-valued correction values, is a new approach to polarization microscopy, and this work is the first demonstration of the correction method.

When correction factors are not applied, the resulting Stokes parameters will not accurately reflect the magnitudes of the polarization components. To illustrate the effects of not addressing correction factors or their spatial distributions, Fig. S8 shows maps of the Stokes parameters S_1 and S_2 for the films presented in Fig. S7 (*i.e.* parameters calculated directly from channel intensities without corrections). The films produce ensemble averaged emission that are orientationally isotropic, which would correspond to Stokes parameters $S_1 = S_2 = 0$. However, all imaging configurations and color channels result in skewed values for the Stokes parameters. Within the red channels, the Stokes parameters are skewed both positively and negatively, depending on the location in the FOV. Such spatial variation demonstrates the need for correction factors to be dependent on the location of the emitter being analyzed.

Propagating the skewness of the Stokes parameters S_1 and S_2, Fig. S9 illustrates the resulting bias of the azimuthal angle ϕ and Stokes polarization parameter p due to the spatial variations of the optical path efficiencies. The bias in p is small for the polarization-only configuration and the red channel. However, the blue channel exhibits values in excess of the maximum modulation depth predicted for a 2D emitter, a condition that should only be available to a 1D emitter (see Fig. S3a and orientation analysis section above).

Optical path calibration measurements of QD films are valid at the red-shifted wavelengths of the films. The spectral terms of the correction factors need to be adjusted for single particle analyses at the appropriate wavelength of the emitter. Figure S10 shows spectral maps of the calibration dataset used to calculate correction factors in the dual-color configuration. From each polarization optical path, red/blue channel pairs determine spectral maps over the FOVs. The ratio of the spectral response functions (see Methods section) utilizes the film wavelength maps to determine the fraction of undetected photons from the correction factor dataset to adjust for the fraction of undetected photons at the wavelength of an emitter of interest. The spectral maps in Fig. S10a are spatially uniform, contrary to the clear spatial heterogeneity of the source maps (the correction factor maps in Fig. S7). Because the spectral maps of the calibration films are uniform, matching an emitter's location within these maps is less significant for the spectral correction, unlike the correction factor maps. Similar to the QD spectral example in Fig. S5, the two S-polarization components and the two P-polarization components are different due to the AOI on the dichroic beamsplitters.

Figure S11 demonstrates the application of correction factors for the orientation calculation of a single QD. The same QD was imaged in both a polarization-only configuration and a dual-color configuration. The top row shows the raw Stokes anisotropy parameters S_1 and S_2 when no corrections are applied. Each channel generates a feature with a different phase (corresponding to different orientation azimuthal angles ϕ) and radius (Stokes polarization

parameter p). For the case of combined red/blue channels, the feature corresponds to the average of the individual components. As expected from the significant skewness in the blue channels (see Fig. S8), the feature is positioned deep into the positive S_1 and S_2 quadrant and is outside the limits of a 2D emitter (red circle). Without correction, the blue channel data cannot be transformed into a polar angle. When the correction factors are applied for the appropriate spatial location of the spot and emission wavelength (bottom row), all channels and imaging configurations produce the feature at the same location in the polarization anisotropy scatter plots. Furthermore, the dual-color measurements that require the more extensive spectral adjustments due to photon losses produce the same results as the polarization-only measurements.

The effects of the correction factors for a several single QDs are summarized in Fig. S12. The before (open circles) and after (crosses) Stokes anisotropy scatter illustrate the systematic skewness of the red and blue channels. Each marker represents the average S_1 and S_2 value from a time-series measurement.

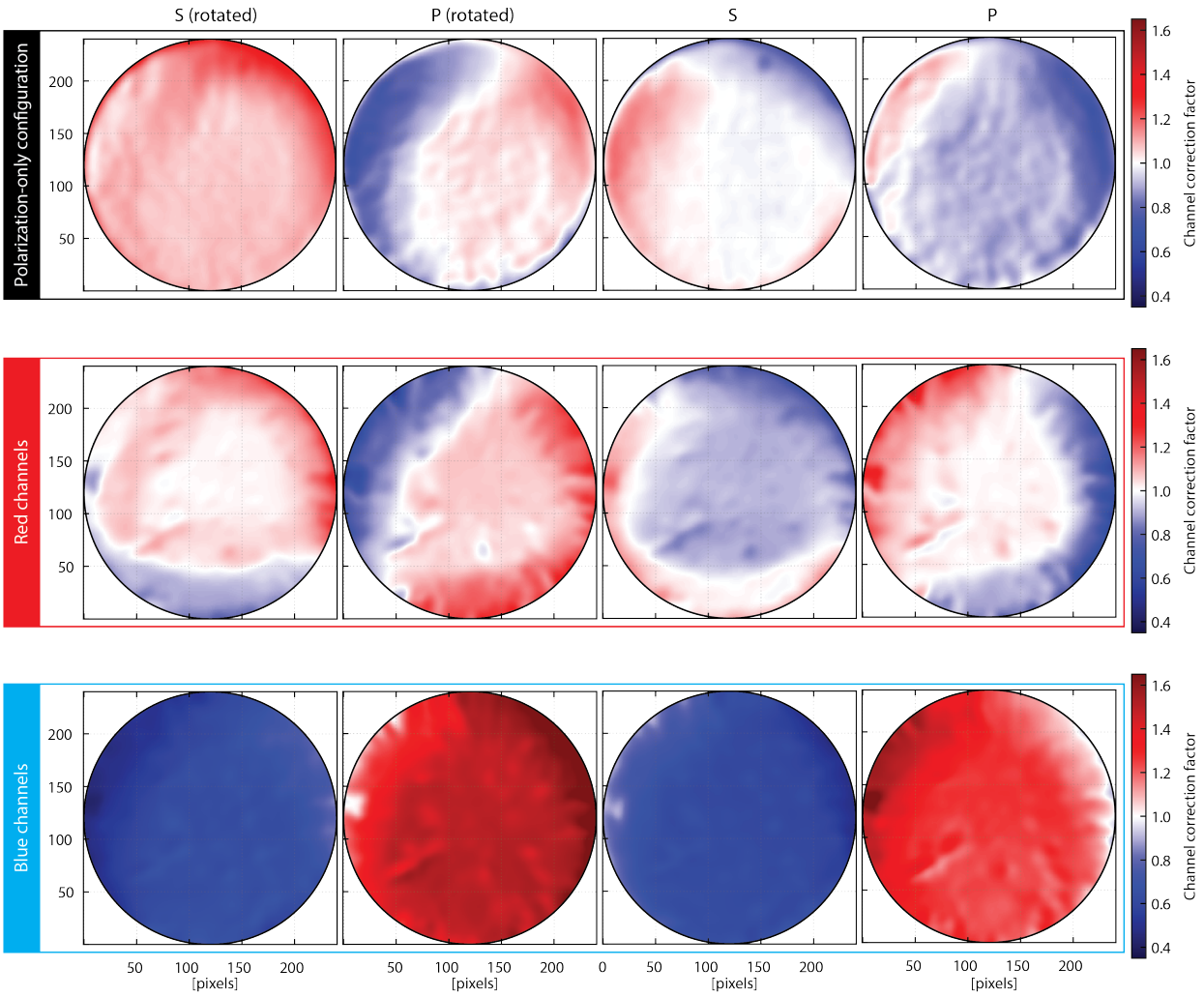

Figure S7: **Correction maps from QD films.** The correction factors $\delta_{i,j}(x, y, \lambda^{\text{film}})$ for various color imaging configurations. Top row: polarization-only configuration without dichroic beamsplitters. Middle row: red channel correction maps for dual-color configuration. Bottom row: blue channel correction maps for dual-color configuration. The correction factors for polarization-only and the red channel of dual-color configurations are similar, but the blue channels require significant corrections. Red map coloring indicates channel efficiency is high and blue map coloring indicates efficiency is low, while white indicates regions where the channel is well-balanced.

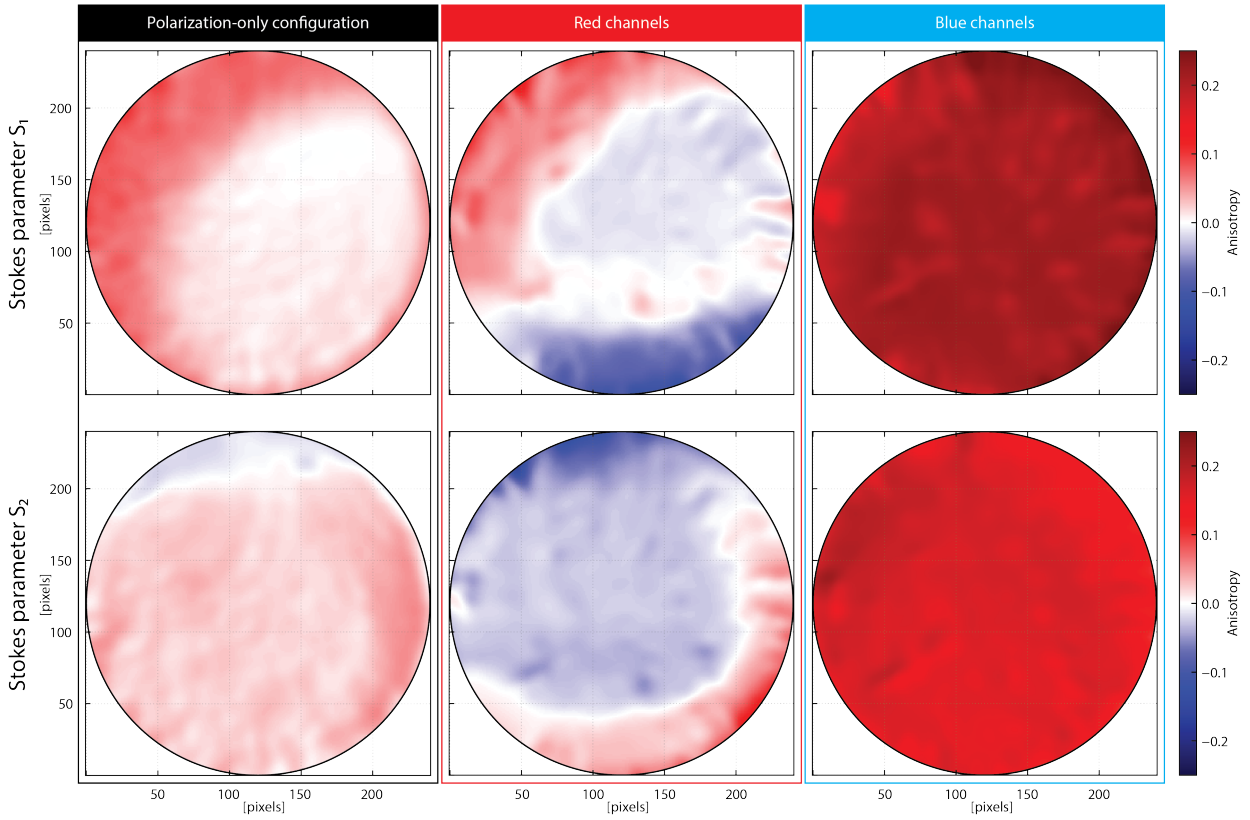

Figure S8: **Raw Stokes parameters of QD film.** The bias of the Stokes parameters S_1 (top row) and S_2 (bottom row) if intensity corrections are not applied. The bias is non-uniform across the FOV and different among the configurations. Strong bias to positive S_1 and S_2 values is present in the blue channels, which would lead to modulation depths not physically possible according to the model to extract the polar angle of a 2D emitter. Bias in polarization-only and the red channel of the dual-color configuration is also present, but less significant.

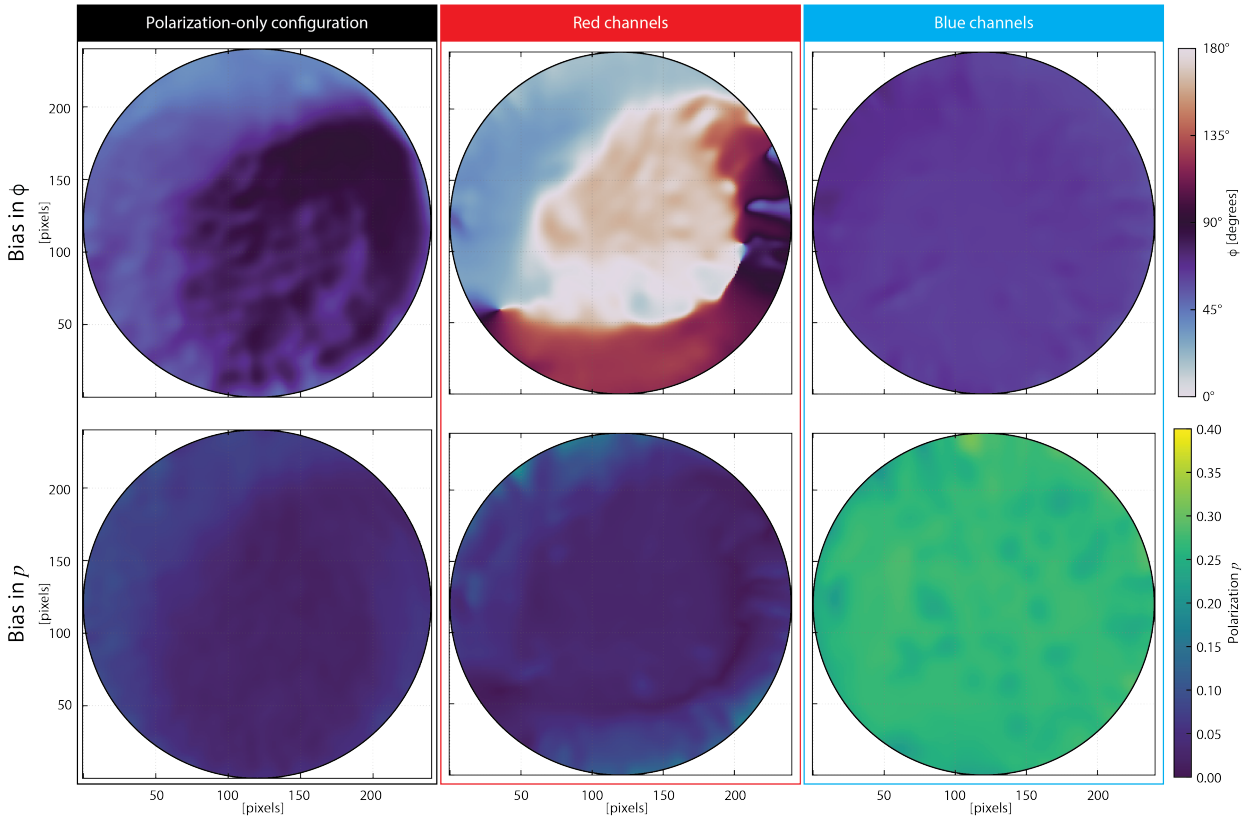

Figure S9: **Orientation bias of QD film.** Calculating the azimuthal angle ϕ from uncorrected intensity information (top row) results in bias among all channels, and is particularly non-uniform for red channels of the dual-color configuration. Bias of the modulation depth p (bottom row) is significant in the blue channel and values exceed the valid modulation depths for the polar angle model of a 2D emitter. The bias in p is relatively uniform in all configurations.

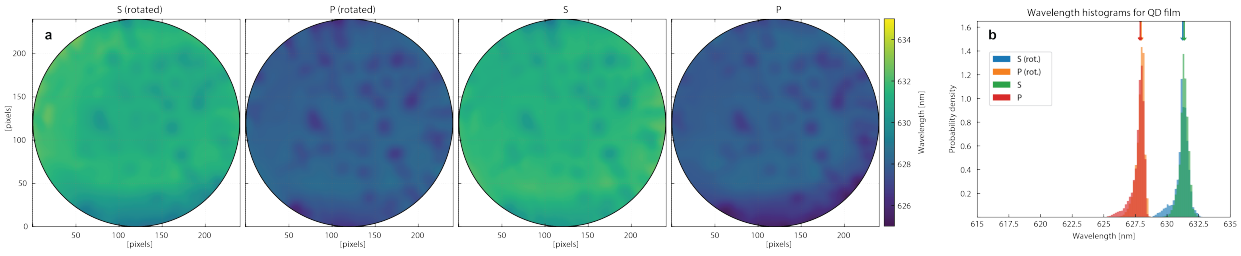

Figure S10: **Spectral maps of QD film. a,** Spectral maps of each polarization channel from a QD film. The spectral signature is uniform across the FOV. Polarization pairs (*e.g.* S rotated and S) estimate the same wavelength, but across pairs (*e.g.* S and P) there is a spectral shift. **b,** Histograms of the spectral maps.

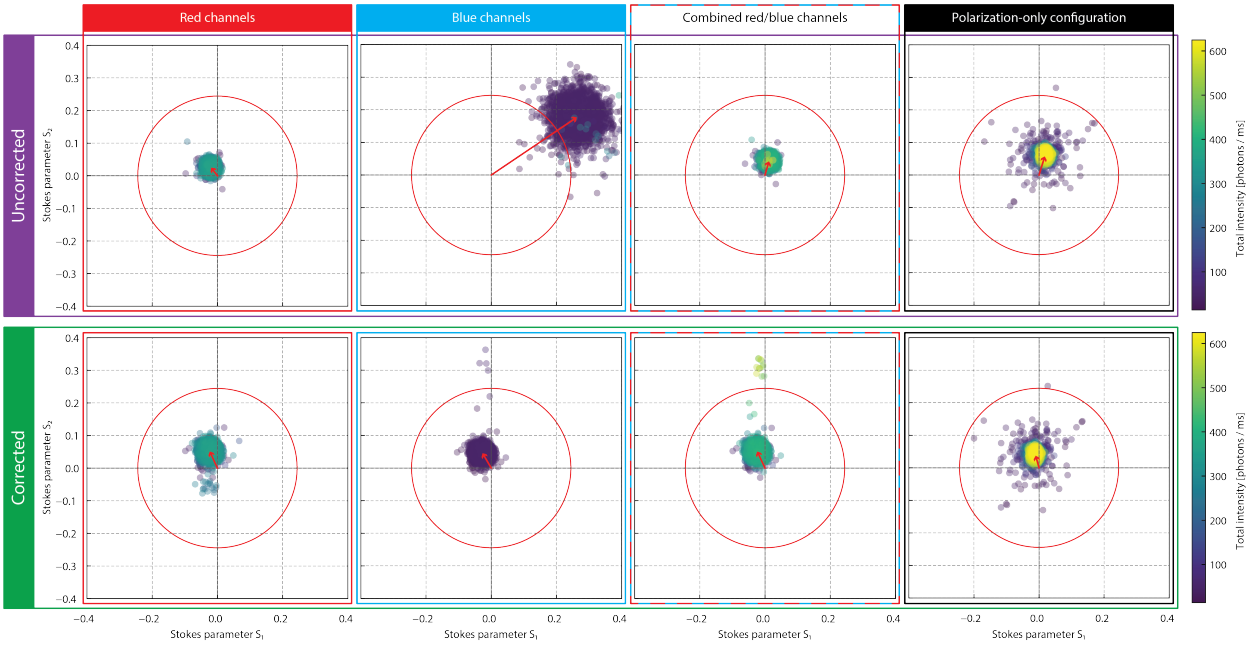

Figure S11: **Application of corrections for a single QD.** Stokes parameter scatter plots of a single QD without (top row) and with (bottom row) the application of correction factors. The combined channel configuration adds red and blue channel intensities together. Without correcting optical path efficiencies, each channel generates different orientations. Applying correction factors results in each channel individually producing the same orientations as the other channels and results are consistent among each configuration.

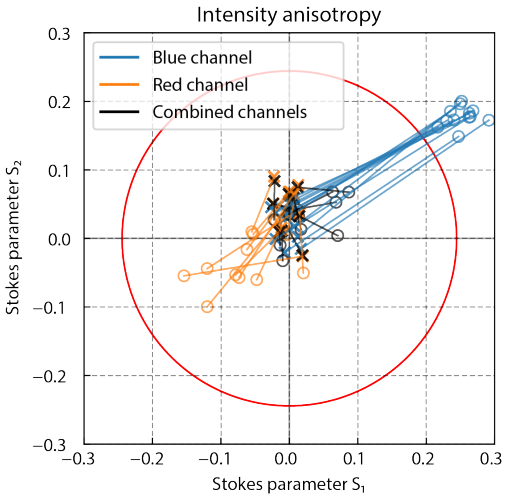

Figure S12: **Corrections for single QDs.** Average Stokes parameters before (open circles) and after (crosses) correction for a collection of single QDs. The systematic bias of the red and blue channels is evident. The markers indicating corrected positions overlap well among the various channels.

VI Localization correction

Emission from dipole emitters can produce asymmetric PSFs that affect localization results[12–14]. While the 2D emission from QDs produces more symmetric PSFs than 1D emitters by mixing basis images, they are similarly prone to localization errors. For single QDs, such localization errors manifests as position offsets. In QD clusters, individual particles may have different orientations that generate unique PSFs, resulting in incorrect relative localizations as the QDs change emission states. These errors produce super-resolution localization maps that are inconsistent with the physical layout of the emitters. Figure S13a–b,d–e show the raw super-resolution localization from each polarization component of a QD cluster (red channels only). Because of dipole effects, each polarization component generates a different map of the cluster as the QDs transition among their emission states.

Several methods have been proposed to correct localization errors from dipole effects. PSF engineering has been used to eliminate the effects of dipole emission by restoring symmetry to the PSFs with additional optics[15, 16]. Recently, Nevskyi, *et al.*[17] identified a simple solution available to detection schemes that separately image orthogonal polarization pairs. Recognizing that there is always one axis of symmetry in a given polarization component, a corrected super-resolution map can be generated by using the coordinates corresponding to the symmetric axes. For example, using the pair of S- and P-polarization components, the x-coordinate is taken from the localization results of the P-polarization component and the y-coordinate is taken from the S-polarization results. For the rotated S- and P-polarization channels, the axes of symmetry are rotated 45°. Thus, the localization results must be transformed into the symmetric coordinate system (x', y'), the valid component identified, and transformed back. The transformation into the primed coordinate system is

$$x' = x \cdot \cos\left(-\frac{\pi}{4}\right) - y \cdot \sin\left(-\frac{\pi}{4}\right)$$
$$y' = x \cdot \sin\left(-\frac{\pi}{4}\right) + y \cdot \cos\left(-\frac{\pi}{4}\right)$$

Figure S13c,f show the corrected localization maps for the same dataset. The corrected super-resolution maps are consistent among the direct and polarization-rotated optical paths. Because two polarization components combine to generate a single localization map, the intensity scales in the corrected images indicate the combined intensities.

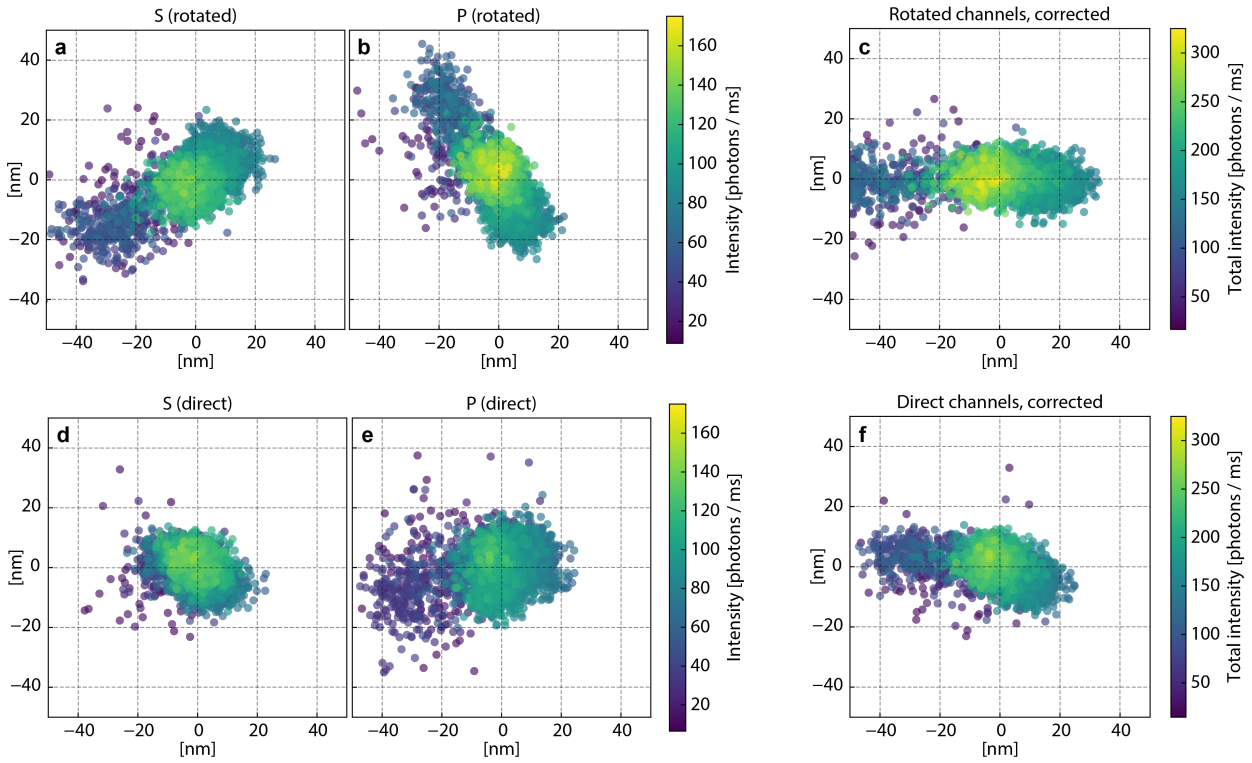

Figure S13: **Localization correction.** **a,** Drift-corrected localization plot for a QD nanoassembly from the red spectral channel of the rotated S polarization optical path. **b,** Localization from the rotated P polarization optical path. Raw localization maps are distorted and inconsistent because of PSF asymmetry. **c,** Corrected localization map using the x' coordinate from the rotated P optical path data and the y' coordinate from the rotated S optical path. **d,** Drift-corrected localization plot for the same QD nanoassembly from the red spectral channel of the S polarization optical path. **e,** Localization fom the rotated P polarization optical path. **f,** Corrected localization map using the x coordinate from the P optical path data and the y coordinate from the S optical path. **c** and **f** depict similar shapes after localization corrections are applied compared to the four different localization maps from the raw localization data.

VII PSF considerations

Byproducts of the localization fitting procedure (see Methods) are residual images of the PSFs for each spot and each polarization component. These images indicate spatially where the 2D pixel-integrated Gaussian PSF underestimates or overestimates the number of photons actually detected. In principle, the residuals could be used in conjunction with a near-focus dipole PSF model to extract orientation[18–20]; however, the high-quality oversampled residuals generated during localization fitting in this work reduce noise by averaging over entire measurements. Dynamic changes to the orientation would require individual frame analysis, but would also be degraded by shot noise noise, amplification noise, and pixelation. Furthermore, aberrations introduce distortions into the image that, if severe, can be challenging to a fitting algorithm.

The residuals of several QDs and QD nanoassemblies are shown in Fig. S14. Although the multiple datasets were acquired over several measurements—and would have minor focal set-points differences—there are common patterns among the individual polarization components. PSF symmetries that the localization correction method takes advantage of are evident: $-45°$ and $45°$ polarization component residuals are symmetric with respect to axes rotated $45°$, and $0°$ and $90°$ residuals are symmetric with respect to the horizontal and vertical directions. However, distortions exist that make each residual unique.

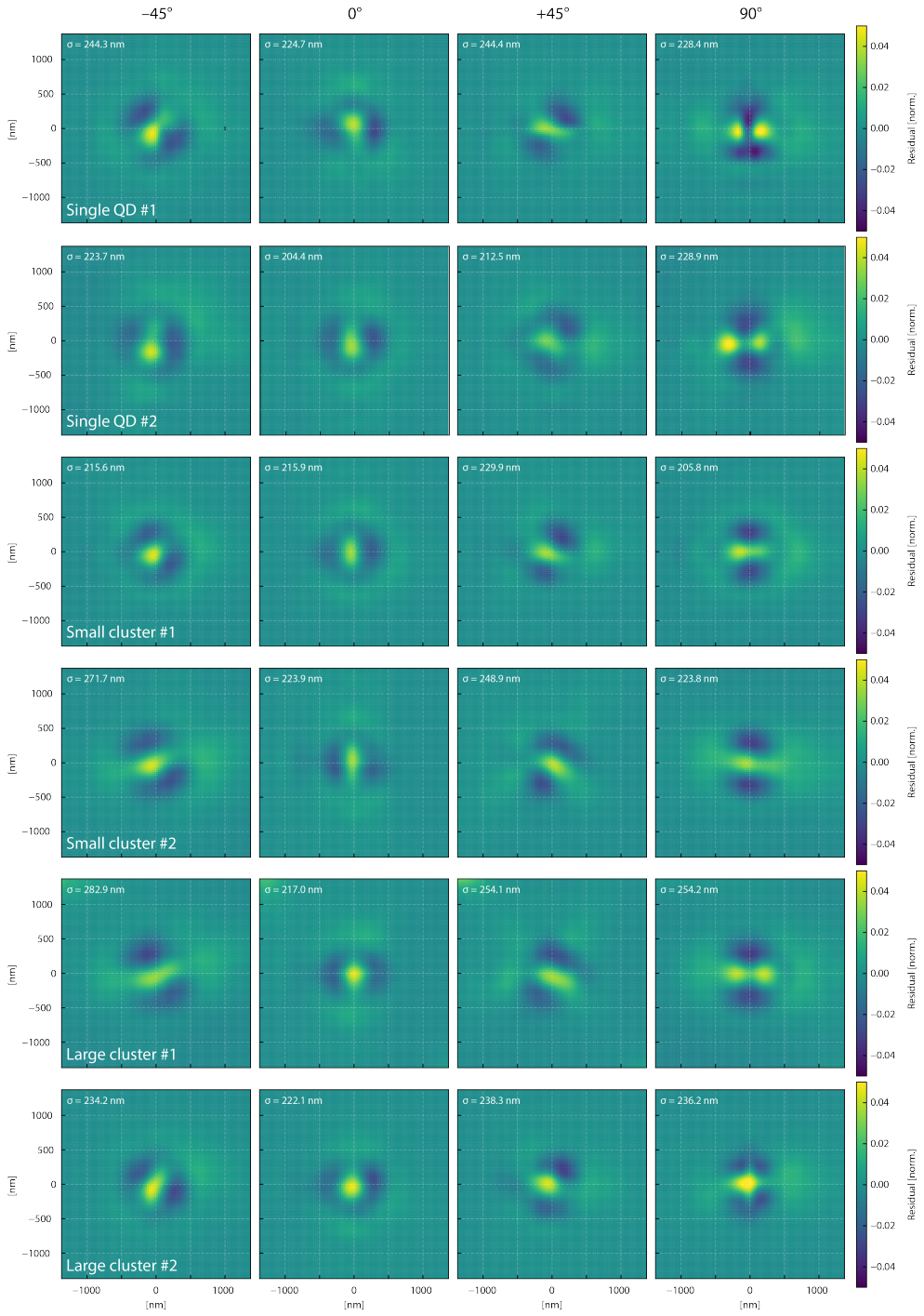

Figure S14: **PSF residuals.** Residuals from red channel images for several QDs and QD nanoassemblies. Each column is a polarization channel and each row a different QD/nanoassembly. The average first-pass PSF fit width σ is indicated for each residual.

VIII Additional examples

The spectral-intensity distribution, orientation, and localization maps for the example nanoassembly in Fig. S13 are shown in Fig. S15. This spot may have been a nanoassembly with low coupling efficiency, a broken nanoassembly with components whose final alignments were different, or a rare example of separate QDs depositing nearby despite sparse coverage in the FOV. The orientation signature displays more variation than the other examples presented, demonstrating the measurement and analysis methods are sensitive to different orientations. The width of the spectral feature was broader than strongly-coupled the QD clusters in the main manuscript.

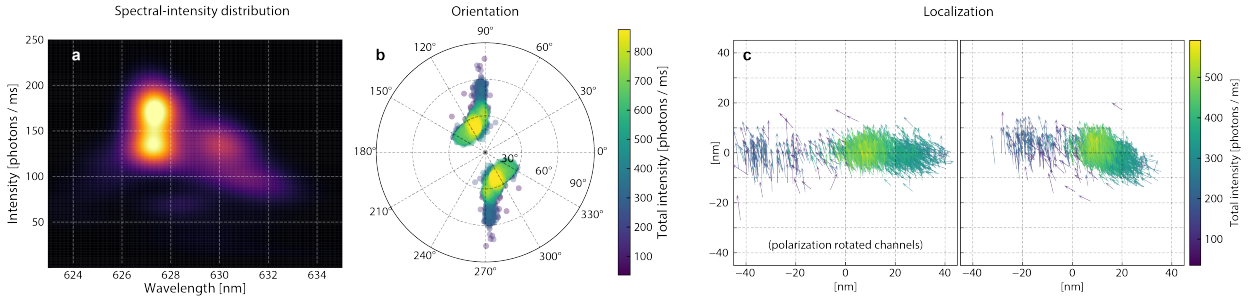

Figure S15: **Alternative cluster example. a–c,** Spectral-intensity distribution, orientation, and localization maps for the QD nanoassembly (same nanoassembly as Fig. S13). The localization plots have been thinned to better visualize the arrow orientations. This is a rare example of a QD nanoassembly that had orientation signatures with dramatically different angles. The different orientations are localized to different spatial regions and correspond to different intensity levels.

An additional interacting large cluster example is shown in Fig. S16. Similar to the large cluster shown in Fig. 4, intensity and wavelength were spatially inhomogeneous, but the polarization signature was uniform. This example showed minor correlation among the azimuthal orientation and the wavelength, as opposed to correlation with the the polar angle in the main text, but this was also a weak correlation.

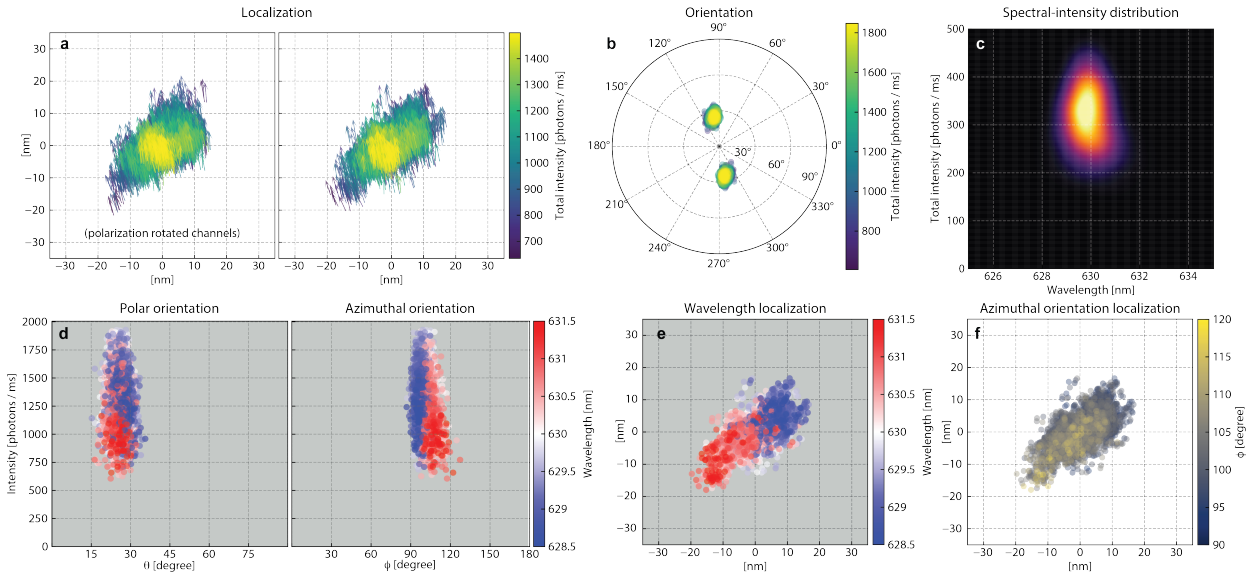

Figure S16: **Alternative large cluster example.**

IX Polar angle wavelength correlation

The correlation between the polar tilt angle and emission wavelength for the large QD nanoassembly example in Fig. 4 is shown in Fig. S17. While there is a correlation between the two emission properties, the weakness of the correlation and broadness of the distributions explain why the polar tilt angle is uniformly distributed spatially whereas the wavelength has distinct short- and long-wavelength sub-regions in the localization plot.

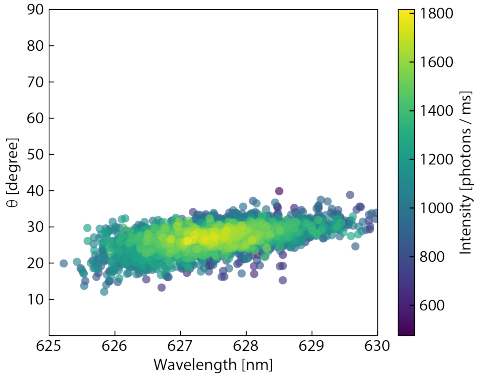

Figure S17: **Polar angle wavelength correlation.** Correlation of polar tilt angle θ with wavelength for large QD nanoassembly.

References

1. Chen, O. *et al.* Compact high-quality CdSe–CdS core–shell nanocrystals with narrow emission linewidths and suppressed blinking. *Nature Materials* **12,** 445 (2013).
2. Lethiec, C. *et al.* Measurement of Three-Dimensional Dipole Orientation of a Single Fluorescent Nanoemitter by Emission Polarization Analysis. *Physical Review X* **4,** 021037 (2014).
3. Koberling, F. *et al.* Fluorescence Anisotropy and Crystal Structure of Individual Semiconductor Nanocrystals. *The Journal of Physical Chemistry B* **107,** 7463–7471 (2003).
4. Schuster, R., Barth, M., Gruber, A. & Cichos, F. Defocused wide field fluorescence imaging of single CdSe/ZnS quantum dots. *Chemical Physics Letters* **413,** 280–283 (2005).
5. Htoon, H., Furis, M., Crooker, S. A., Jeong, S. & Klimov, V. I. Linearly polarized 'fine structure' of the bright exciton state in individual CdSe nanocrystal quantum dots. *Physical Review B* **77,** 035328 (2008).
6. Cyphersmith, A. *et al.* Disentangling the role of linear transition dipole in band-edge emission from single CdSe/ZnS quantum dots: Combined linear anisotropy and defocused emission pattern imaging. *Applied Physics Letters* **97,** 121915 (2010).
7. Li, J., Kwok, K.-C. & Cheung, N.-H. Determination of the Dipole Geometry of Fluorescent Nanoparticles Using Polarized Excitation and Emission Analysis. *Applied Spectroscopy* **70,** 302–311 (2016).
8. Talapin, D. V. *et al.* CdSe/CdS/ZnS and CdSe/ZnSe/ZnS Core-Shell-Shell Nanocrystals. *The Journal of Physical Chemistry B* **108,** 18826–18831 (2004).
9. Smith, A. M., Mohs, A. M. & Nie, S. Tuning the optical and electronic properties of colloidal nanocrystals by lattice strain. *Nature Nanotechnology* **4,** 56–63 (1 2009).
10. Ryan, D. P. *et al.* A framework for quantitative analysis of spectral data in two channels. *Applied Physics Letters* **117,** 024101 (2020).
11. Zhu, M., Zhou, J., Hu, Z., Qin, H. & Peng, X. Effects of Local Dielectric Environment on Single-Molecule Spectroscopy of a CdSe/CdS Core/Shell Quantum Dot. *ACS Photonics* **5,** 4139–4146 (2018).
12. Enderlein, J., Toprak, E. & Selvin, P. R. Polarization effect on position accuracy of fluorophore localization. *Optics Express* **14,** 8111 (2006).
13. Backlund, M. P., Lew, M. D., Backer, A. S., Sahl, S. J. & Moerner, W. E. The Role of Molecular Dipole Orientation in Single-Molecule Fluorescence Microscopy and Implications for Super-Resolution Imaging. *ChemPhysChem* **15,** 587–599 (2014).
14. Furubayashi, T. *et al.* Nanometer Accuracy in Cryogenic Far-Field Localization Microscopy of Individual Molecules. *The Journal of Physical Chemistry Letters* **10,** 5841–5846 (2019).

15. Lew, M. D. & Moerner, W. E. Azimuthal Polarization Filtering for Accurate, Precise, and Robust Single-Molecule Localization Microscopy. *Nano Letters* (2014).

16. Backlund, M. P. *et al.* Removing orientation-induced localization biases in single-molecule microscopy using a broadband metasurface mask. *Nature Photonics* **10,** 459–462 (7 2016).

17. Nevskyi, O., Tsukanov, R., Gregor, I., Karedla, N. & Enderlein, J. Fluorescence polarization filtering for accurate single molecule localization. *APL Photonics* **5,** 061302 (2020).

18. Böhmer, M. & Enderlein, J. Orientation imaging of single molecules by wide-field epifluorescence microscopy. *Journal of the Optical Society of America B* **20,** 554–559 (2003).

19. Aguet, F., Geissbühler, S., Märki, I., Lasser, T. & Unser, M. Super-resolution orientation estimation and localization of fluorescent dipoles using 3-D steerable filters. *Optics Express* **17,** 6829 (2009).

20. Backer, A. S. & Moerner, W. E. Determining the rotational mobility of a single molecule from a single image: a numerical study. *Optics Express* **23,** 4255–4276 (2015).